Materials Research. 2026; 29(suppl. 2): e20260172
DOI: https://doi.org/10.1590/1980-5373-MR-2026-0172

Isotopic Characterization of Apatite and Zircon: Crystallographic Integrity, Etching Effects, and Geochronological Implications

***Camila Durães F. dos Santos*[a*], *Pedro Brandão Christante*[a], *Luana Rosa Bilac Caetano*[a], *Elton L. Dantas*[b], *Pieter Vermeesch*[c], *Carlos Alberto Tello Sáenz*[a]**

[a]*Universidade Estadual Paulista (UNESP), Faculdade de Ciências e Tecnologia, Departamento de Física, Presidente Prudente, SP, Brasil.*
[b]*Universidade de Brasília (UnB), Instituto de Geociências, Brasília, DF, Brasil.*
[c]*University College London (UCL), Department of Earth Sciences, London, United Kingdom.*

Received: May 14, 2026; Revised: August 13, 2026; Accepted: September 06, 2026

The effects of chemical zoning and radiation damage on U-Pb isotopic behavior were investigated in apatite from the Borborema Province and zircon from the Carajás Province, Brazil, using optical microscopy and LA-ICP-MS. Sample BJ19C, characterized by homogeneous fission-track distributions, yielded a concordia age of 569.6 ± 1.7 Ma, however, individual analyses showed 87.7 Ma of age dispersion and intra-grain offsets of up to 29.2 Ma. In contrast, chemically zoned CEBP035 yielded a concordia age of 538.6 ± 1.2 Ma and intra-grain age offsets of up to 85.6 Ma. A separate Raman case study of a single representative grain (CEBP035-G01) showed broader ν_1 (PO_4) bands in U-rich domains, with FWHM increasing from 3.2 to 4.4 cm^{-1}, while the phosphate framework remained largely crystalline. For zircons, etched aliquots exhibited distinct spot distributions along similarly oriented discordia trends. Isotopic patterns were sample-dependent: sample C16 showed tighter regression alignment, C20 displayed a wider spatial distribution, and C23 showed no statistical change. Etched and unetched populations yielded equivalent upper-intercept ages. The results indicate that chemical heterogeneity and radiation damage contribute to U-Pb dispersion in apatite and zircon, while chemical etching modifies the analytical response of metamict zircon without systematically changing the inferred crystallization age.

Keywords: *Apatite, Zircon, Lattice stability, Radiation damage, Raman spectroscopy, U-Pb geochronology.*

1. Introduction

The isotopic systems of accessory minerals, specifically apatite and zircon, are primary indicators of the thermal and chronological evolution of crustal rocks. These minerals incorporate trace amounts of uranium (^{238}U and ^{235}U) into their lattices, which undergo decay chains involving sequential alpha and beta emissions that ultimately produce radiogenic lead isotopes (^{206}Pb and ^{207}Pb, respectively), alongside spontaneous fission of ^{238}U, which generates linear structural defects known as fission-tracks[1-8]. The integration of these chronometers enables the reconstruction of complex time-temperature (t-T) paths, provided the host mineral retains its structural integrity[9,10]. Over geological timescales, accumulated radiation damage - primarily driven by the recoil of heavy daughter nuclei during alpha decay - progressively destroys the crystalline lattice, a process known as metamictization[8,11]. In highly retentive and uranium-rich zircon, progressive radiation damage eventually reaches the percolation threshold[8], connecting previously isolated amorphous domains into three-dimensional damage networks that extend throughout the crystal[8,12,13]. This structural collapse reduces mineral density, increases elemental diffusivity[11,12], and renders metamict zones highly susceptible to open-system behavior and radiogenic Pb loss, as well as severe analytical artifacts during laboratory etching[14]. Conversely, low to moderate radiation doses in apatite tend to form isolated defects that act as structural traps rather than interconnected pathways[15,16].

A primary challenge in accessory mineral characterization is quantifying how crystal lattices respond to both internal stressors (radiation damage, chemical zoning) and external pre-treatments (chemical etching). Although essential for optical fission-track revelation, etching interacts preferentially with structurally compromised domains rather than reacting uniformly, thereby modifying the analytical surface[5,17,18]. During in situ U-Pb analyses by LA-ICP-MS, variable lattice integrity complicates matrix-matched standardization[14,19] by inducing variable laser ablation rates[19] and preferential isotopic leaching. Non-destructive characterization techniques such as Raman spectroscopy provide an essential means of evaluating crystallographic order[4,20-22]; however, the decoupling between localized chemical variations—such as uranium enrichment—and physical lattice stability remains insufficiently constrained. To examine these contrasting structural responses, we evaluate chemically zoned apatites from the

*e-mail: camila.duraes@unesp.br
Associate Editor: Luis Cabral.
Editor-in-Chief: Luiz Antonio Pessan.

São José do Campestre Domain (Borborema Province)[13,23-25], where the lattice framework remains largely intact despite internal chemical gradients, alongside highly metamict Archean zircons from the Carajás Mineral Province[26], where billions of years of damage facilitate open-system behavior during chemical pre-treatment[17,18,27].

Despite the widespread application of etching for fission-track revelation and structural characterization, a critical knowledge gap remains regarding how chemical pre-treatments interact with variable degrees of radiation damage and chemical zoning to influence subsequent in situ U-Pb analyses. While etching preferentially dissolves radiation-damaged domains[17,18], the extent to which this chemical pre-treatment modifies the analytical surface, alters elemental/isotopic ratios, or biases age interpretations across minerals with contrasting radiation histories has not been systematically evaluated. This knowledge gap is particularly critical when structural degradation and isotopic behavior become partially decoupled in minerals exhibiting heterogeneous radionuclide distributions or complex metamictization histories[4,8].

This study investigates the isotopic response of apatite and zircon to distinct structural conditions and chemical pre-treatments using in situ LA-ICP-MS U-Pb geochronology integrated with optical and structural characterization. For the Borborema Province apatites, U-Pb ages, uranium concentrations, and fission-track distributions are evaluated across multiple crystal populations to determine whether intra-grain uranium zoning and track-density heterogeneities promote age discordance, complemented by high-resolution Raman mapping on a representative zoned grain to assess localized strain versus lattice preservation. For the highly metamict Archean zircons from the Carajás Province, we investigate how etching influences U-Pb isotopic systematics in severely radiation-damaged lattices by evaluating discordia regressions and upper-intercept ages obtained from etched and unetched populations. By integrating these analytical approaches, this study investigates how differential lattice degradation influences isotopic systematics and provides a framework for interpreting U-Pb data from minerals with complex internal architectures.

2. Experimental Procedure

2.1. Sample selection and preparation

The study focused on accessory minerals from two distinct geological settings in Brazil: (i) apatite crystals from the São José do Campestre Tectonic Domain (Borborema Province), samples CEBP035 and BJ19C, and (ii) Archean zircon grains from the Carajás Mineral Province (samples C16, C20 and C23).

Minerals were concentrated using standard gravimetric and magnetic separation techniques at the University of Brasília (UnB). The grains were mounted in epoxy and Teflon, polished to expose their internal geometry, and screened via optical microscopy to identify inclusion-free domains and representative growth zoning.

Standard etching protocols were applied to reveal internal fission tracks in apatite. Apatites were etched in 5.5 M HNO_3 for 20 s at 21 °C[5,28]. For zircon, etching was performed using a KOH-NaOH eutectic mixture at 225 °C for 4 h to 10 h[29]. In addition to the etched crystals, a separate set of unetched zircon grains was prepared. Both etched and unetched populations were subsequently analyzed via LA-ICP-MS to compare the isotopic response of the metamict domains. This comparative strategy builds upon the analytical framework proposed by Azevedo[13] and Resende et al.[18], utilizing etching as a physical screening tool to differentiate structurally preserved, closed-isotopic-system regions from highly damaged zones, either within the same grain or across different grains, prior to isotopic analysis.

2.2. Raman spectroscopy

Structural characterization was performed using a Renishaw inVia Raman spectrometer equipped with a 633 nm He-Ne laser. Raman measurements were acquired using 20× and 50× microscope objectives, depending on the spatial scale of the measurement. The laser power was set to 50 mW, and spectra were collected in static acquisition mode with an integration time of approximately 0.1 s per spectrum and a single accumulation.

High-resolution Raman mapping was performed on an unetched apatite grain from sample CEBP035 (grain G01) using a spatial step size of 1 × 1 µm. Approximately 7000 spectra were acquired across the mapped area. The effective spectral resolution of the system was approximately 2 cm^{-1}, as empirically determined from measurements of a crystalline silicon reference standard.

Spectral analysis focused on the ν_1 (PO_4) symmetric stretching mode near 965 cm^{-1}. Individual Raman bands were fitted in Python using a pseudo-Voigt profile. Only fits with a coefficient of determination (R^2) greater than 0.90 were retained for subsequent analysis. An additional quality-control criterion was applied to the fitted full width at half maximum (FWHM): spectra yielding FWHM values $\leq$2 cm^{-1} or $\geq$20 cm^{-1} were excluded because such values approach the instrumental resolution or are more likely to represent poorly constrained fits, spectral artifacts, or non-representative signals. The retained fitted peak positions, intensities, and FWHM values were used to construct two-dimensional Raman maps and evaluate spatial variations in the crystallographic response of the apatite lattice.

2.3. LA-ICP-MS isotopic analysis

U-Pb geochronology and trace element mapping were conducted at the London Geochronology Centre, University College London (UCL). The analytical session utilized a New Wave NWR 193 nm excimer laser ablation system coupled to an Agilent 7700 quadrupole ICP-MS. Ablation was performed with a spot size of 30 µm, a repetition rate of 10 Hz, and a fluence of approximately 2.5 J/cm^2.

For apatite analyses, the Madagascar apatite was used as the primary reference material, while Durango and NIST SRM 612 were used as secondary standards to monitor accuracy and instrumental drift[14,30-32]. For zircon, the Plešovice zircon served as the primary standard[33], supported by the 91500 zircon[34] and NIST SRM 612 as secondary reference materials.

Data reduction was performed using the KJ software package[35]. Corrected isotopic ratios (e.g., $^{206}Pb/^{238}U$ and $^{207}Pb/^{206}Pb$) were exported to IsoplotR[36] for geochronological data analysis, age calculations, and concordia/discordia visualization.

Common-Pb correction for apatite was performed using isochron regression, and Concordia ages were calculated using Wetherill concordia diagrams. For the Archean zircon dataset, upper-intercept ages were determined from linear discordia regressions on Wetherill concordia diagrams.

3. Results and Discussion

3.1. Apatite etching screening

Isotopic characterization via LA-ICP-MS revealed distinct chemical signatures and U-Pb isotopic behaviors between the analyzed apatite samples. While both samples provided sufficient ion counts for geochronological dating, their internal distributions of U and Th demonstrate contrasting zoning patterns. Sample BJ19C (Figure 1A) exhibits relatively uniform fission-track distributions across crystal surfaces, indicating an absence of steep internal uranium gradients. In contrast, sample CEBP035 (Figure 1B) displays marked track-density heterogeneity, with optical evidence of localized variations spatially associated with uranium-enriched domains.

It is important to clarify the distinct methodological role of etching (5.5 M HNO_3 for 20 s at 21 °C) in apatite characterization. Unlike the aggressive eutectic melt etching applied to metamict zircons, etching in apatite was not intended to physically alter, restore, or systematically shift U-Pb isotopic trajectories. Instead, its primary value for U-Pb geochronology lies in acting as a pre-analytical optical screening tool. By revealing spontaneous fission-track distributions, etching visually exposes the internal architecture of the crystal, highlighting marked intra-grain zoning and track halos in sample CEBP035 while confirming relative homogeneity in optical fission-track density in sample BJ19C. This visual revelation provides essential spatial context prior to in situ LA-ICP-MS analysis, enabling targeted spot placement across distinct compositional domains rather than unguided sampling.

3.2. BJ19C apatite sample

Visually, sample BJ19C displays a relatively uniform distribution of spontaneous fission tracks, lacking the steep density gradients or localized halos that will be addressed in the subsequent analysis of sample CEBP035. However, quantitative LA-ICP-MS microanalyses reveal subtle to moderate intra-grain uranium variations (with a maximum intra-grain variation of 74.22 ppm in grain G77). While these variations do not produce macroscopic track-density zoning, they demonstrate that micro-scale elemental variations exist even in optically homogeneous crystals.

Despite the absence of steep chemical zoning, the U-Pb dataset displays broader age dispersion than expected from analytical uncertainties alone (535.4 ± 14.1 to 623.1 ± 15.0 Ma). Consequently, the analyzed apatite population cannot be considered statistically homogeneous, reflecting intrinsic sample-scale variability or the sampling of micro-domains with subtly distinct isotopic histories.

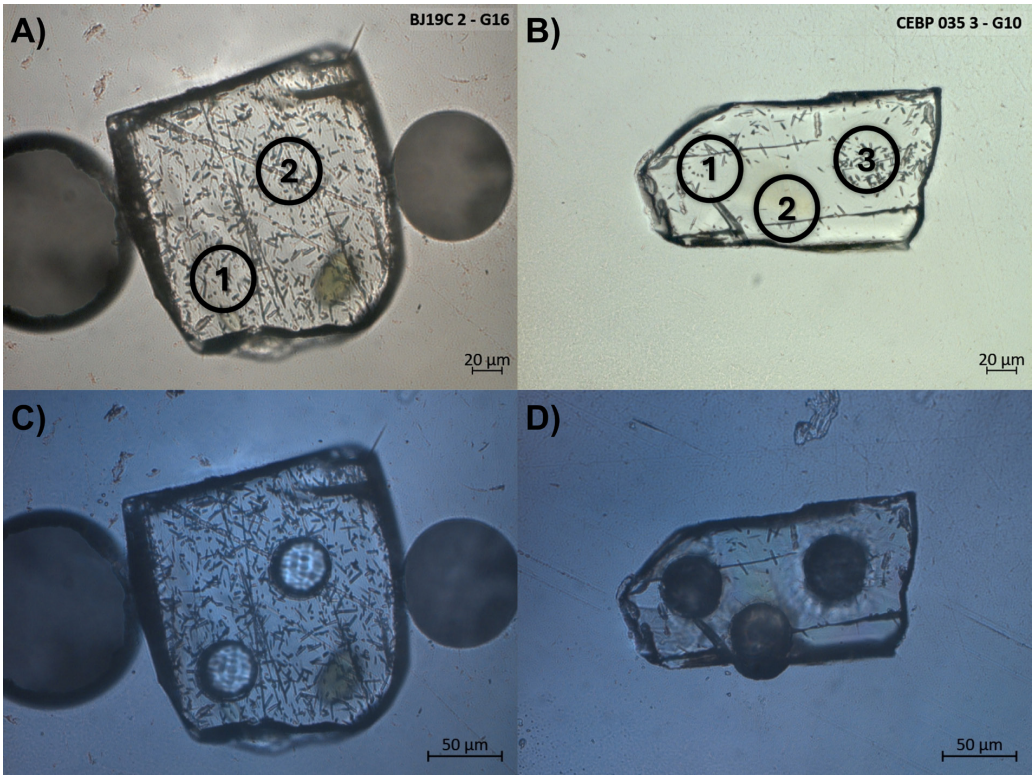


Figure 1. Optical photomicrographs of etched apatite grains under transmitted light. (A) Grain G16 (Sample BJ19C) displaying a homogeneous distribution of spontaneous fission tracks. (B) Grain G10 (Sample CEBP035) exhibiting marked track density zoning. Numbered circles indicate the targeted LA-ICP-MS analytical spots. (C) and (D) show the respective grains after LA-ICP-MS analysis, where the resulting ablation pits are visible.

Beyond the general intra-grain observations, individual grain behaviors from representative targets further illustrate this relationship (Table 1; see Supplementary Table S1 for the complete dataset of all analyzed BJ19C grains). For instance, multi-spot measurements in grain G03 reveal a two-fold variation in uranium content between Spot 1 (63.99 ppm) and Spot 2 (30.69 ppm), which translates into a minor age shift (535.4 ± 14.1 Ma vs. 552.2 ± 14.7 Ma) overlap within the reported 2σ uncertainties. Similarly, grain G15 shows a moderate variation in U concentrations (20.67 to 49.31 ppm) accompanied by an intra-grain age variation from 561.7 ± 10.9 Ma to 590.9 ± 13.3 Ma. In single-spot analyses such as grains G04 and G44, uranium contents cluster tightly around 49-54 ppm with U-Pb ages yielding 581.3 ± 13.9 Ma and 560.6 ± 13.4 Ma, respectively. These representative data confirm that, while minor geochemical fluctuations exist between individual ablation spots, U and Th abundances across BJ19C remain less heterogeneous than in CEBP035, without triggering drastic isotopic decoupling at the single-grain scale.

3.3. CEBP035 apatite sample

Visually, sample CEBP035 presents a clear contrast to BJ19C, exhibiting pronounced intra-grain fission-track zoning and halos under transmitted light (Figures 1B and 2). These optical features suggest steep internal uranium gradients prior to laser ablation, where regions of high track density point to localized U-enriched domains.

Table 1. Representative LA-ICP-MS analytical data for selected apatite grains from sample BJ19C.

Grain - Spot	U (ppm)	Th (ppm)	U-Pb Age (Ma ±2σ)	$^{238}U/^{206}Pb$	$^{207}Pb/^{206}Pb$
G03 - 1	63.99	34.62	535.4 ± 14.1	10.821	0.079
G03 - 2	30.69	14.50	552.2 ± 14.7	9.318	0.112
G04 - 1	54.36	19.40	581.3 ± 13.9	8.832	0.110
G15 - 1	20.67	13.34	561.7 ± 10.9	6.408	0.190
G15 - 2	49.31	39.80	590.9 ± 13.3	8.137	0.125
G16 - 1	55.03	19.83	568.8 ± 11.9	8.052	0.139
G16 - 2	63.45	24.42	585.9 ± 12.3	8.017	0.131
G36 - 1	54.11	25.08	560.0 ± 12.3	8.501	0.131
G44 - 1	49.18	29.95	560.6 ± 13.4	8.943	0.118

Note: U and Th concentrations were obtained by LA-ICP-MS. U-Pb ages are reported with 2σ absolute analytical uncertainties. The full dataset with $^{207}Pb/^{235}U$ and $^{206}Pb/^{238}U$ ratios is provided in Supplementary Table S1.

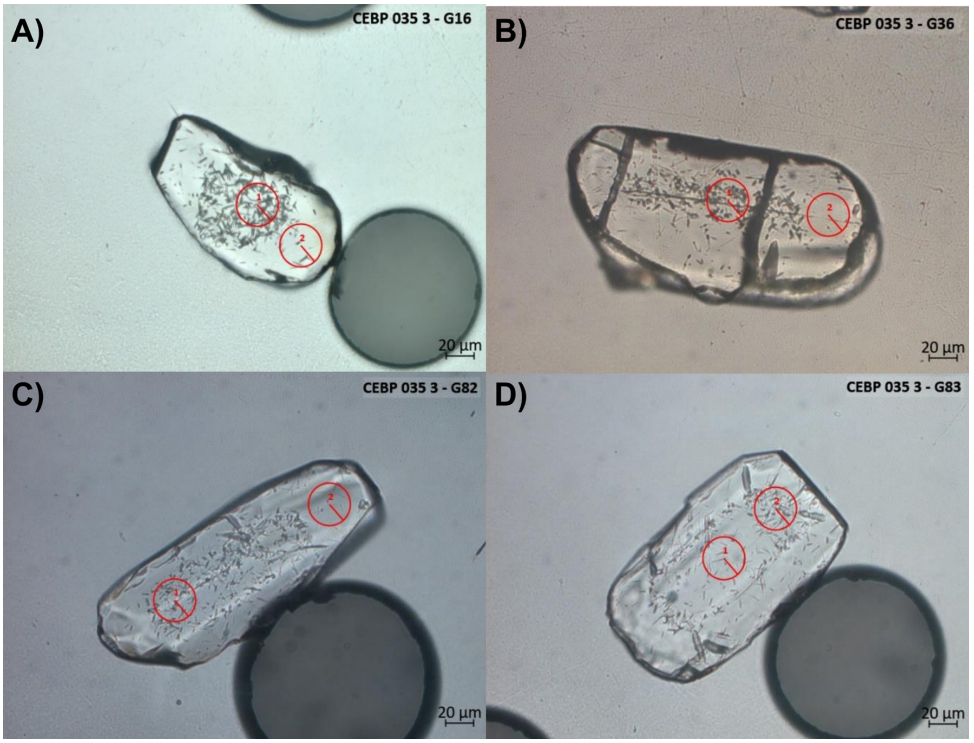


Figure 2. Optical photomicrographs of etched apatite grains from sample CEBP035 showing intra-grain variations in fission-track density associated with uranium zoning. (A) Grain G16, (B) grain G36, (C) grain G82, and (D) grain G83. Numbered circles indicate the LA-ICP-MS analytical spots.

Quantitative LA-ICP-MS microanalyses confirm this chemical heterogeneity across both sample and single-crystal scales. Across the complete CEBP035 dataset (Supplementary Table S2), uranium concentrations span more than two orders of magnitude (5.94 to 329.79 ppm). At the single-grain scale, U and Th concentrations frequently fluctuate by factors of 2 to 4, reaching an extreme intra-grain U variation of 288.93 ppm in grain G06 (40.86 ppm at Spot 1 vs. 329.79 ppm at Spot 2). Consequently, this localized chemical zoning induces significant intra-grain isotopic variability, driving a broad total sample-scale age dispersion of 127.3 Ma (487.9 to 614.5 Ma).

Individual grain behaviors from representative targets illustrate how these chemical gradients dictate isotopic response (Table 2; all analyzed spots are listed in Supplementary Table S2). In grain G10 (Figure 1B), uranium concentrations double from 57.06 ppm (Spot 1) to 112.19 ppm (Spot 3), closely tracking optical fission-track accumulation.

Pronounced intra-grain variation is further exemplified by grains G16, G36, and G82 (Figure 2A-C), where U concentrations vary substantially between ablation spots (e.g., 115.45 to 192.13 ppm in G82), producing corresponding intra-grain age offsets. The most distinct optical-geochemical coupling occurs in grain G83 (Figure 2D), where a four-fold increase in uranium content from Spot 1 (58.94 ppm, halo center) to Spot 2 (232.00 ppm, maximum track accumulation zone) coincides with a localized intra-grain age variation (549.9 ± 14.1 Ma vs. 529.4 ± 13.2 Ma). Maximum intra-grain age offsets across the sample reach up to 85.6 Ma in grain G31-1 (614.5 ± 15.6 Ma vs 528.9 ± 13.2 Ma). Collectively, these observations demonstrate that steep, localized uranium enrichment is associated with notable isotopic disturbance and age dispersion within individual crystals.

3.4. U-Pb geochronology of apatite

The sample–scale U–Pb isotopic distributions and precision patterns for both apatite samples are illustrated in the Wetherill concordia diagrams (Figure 3). While both samples yield Neoproterozoic concordia ages, they exhibit fundamentally distinct degrees of internal isotopic variance and analytical dispersion.

Sample BJ19C (Figure 3A) yields a concordia age of 569.6 ± 1.7 Ma with an extremely low Mean Square Weighted Deviation (MSWD = 0.007). This low MSWD does not indicate isotopic homogeneity across individual domains; rather, it reflects two–dimensional statistical under-dispersion on the Wetherill plot, driven by large relative uncertainties on $^{207}Pb/^{235}U$ ratios that fully encompass the observed data spread. Despite this low MSWD, single-spot analyses span an age range of 87.7 Ma. In contrast, sample CEBP035 (Figure 3B) yields a younger concordia age of 538.6 ± 1.2 Ma (MSWD = 0.22), exhibiting broader overall scatter driven by steep internal uranium gradients and localized radiation-induced disturbances.

In both samples, the color-coded scale represents the uranium concentration (U, ppm) of each analytical spot, indicating a relationship between uranium concentration and analytical precision (Figure 3). Lighter-colored ellipses correspond to domains with lower uranium contents, where lower isotopic signal intensities during LA–ICP–MS measurement result in higher relative analytical uncertainties producing a pronounced horizontal expansion of error ellipses along the $^{207}Pb/^{235}U$ axis. Conversely, darker-colored ellipses correspond to higher uranium concentrations, yielding stronger isotopic signals and tighter, more precisely constrained error ellipses.

Table 2. Representative LA-ICP-MS analytical data for selected grains from sample CEBP035.

Grain - Spot	U (ppm)	Th (ppm)	U-Pb Age (Ma $\pm 2\sigma$)	$^{238}U/^{206}Pb$	$^{207}Pb/^{206}Pb$
G10 - 1	57.06	35.18	545.7 ± 13.3	9.940	0.098
G10 - 2	12.26	6.09	547.8 ± 11.1	6.095	0.207
G10 - 3	112.19	123.54	535.7 ± 13.4	11.233	0.067
G16 - 1	111.02	120.17	562.4 ± 13.6	10.198	0.081
G16 - 2	128.01	135.57	541.8 ± 15.3	11.453	0.057
G31 - 1	70.44	72.00	614.5 ± 15.6	8.964	0.090
G31 - 2	162.58	204.70	528.9 ± 13.2	11.940	0.051
G31 - 3	18.08	19.56	558.2 ± 12.6	7.246	0.168
G36 - 1	140.93	199.79	550.4 ± 14.0	11.380	0.054
G36 - 2	115.29	145.92	545.6 ± 14.0	11.269	0.060
G54 - 1	94.16	86.78	559.6 ± 14.1	10.498	0.074
G54 - 2	77.77	84.76	545.6 ± 13.8	10.570	0.080
G61 - 1	28.81	42.88	545.4 ± 13.3	8.656	0.135
G61 - 2	29.25	46.67	546.5 ± 13.4	8.738	0.132
G70 - 1	70.47	104.04	545.7 ± 14.4	10.777	0.074
G70 - 2	87.55	116.38	556.4 ± 14.0	10.281	0.082
G82 - 1	192.13	195.98	537.2 ± 13.5	11.306	0.064
G82 - 2	115.45	123.17	531.4 ± 13.5	11.013	0.076
G83 - 1	58.94	49.76	549.9 ± 14.1	9.924	0.096
G83 - 2	232.00	239.52	529.4 ± 13.2	11.406	0.066

Note: U and Th concentrations were obtained by LA-ICP-MS. U-Pb ages are reported with 2σ absolute analytical uncertainties. The full dataset with $^{207}Pb/^{235}U$ and $^{206}Pb/^{238}U$ ratios is provided in Supplementary Table S2.

This relationship explains why sample BJ19C (~20–150 ppm U) forms a tight, high-precision cluster, whereas low-U domains in CEBP035 (down to 5.94 ppm U) display distinctly elongated, low-precision ellipses.

3.5. Raman apatite case study

To investigate whether intra-grain uranium variations detected by LA-ICP-MS correlate with localized crystal lattice strain, apatite grain CEBP035-G01 was selected for high-resolution multi-analytical characterization (Figure 4). Transmitted-light imaging (Figure 4A) outlines the crystal morphology and the two LA-ICP-MS ablation spots targeting contrasting chemical domains (~146 ppm U at Spot G01-1 vs. ~28.7 ppm U at Spot G01-2). Cathodoluminescence (CL) imaging prior to isotopic analysis (Figure 4B) revealed subtle spatial variations in luminescence intensity across the grain, highlighting mild internal chemical heterogeneity between these domains. 2D Raman spectroscopic mapping of signal intensity (Figure 4C), FWHM (Figure 4D), and peak position shifts (Figure 4E) further provides a spatial bridge between this internal chemical zoning and crystal lattice integrity.

Due to the overall low cathodoluminescence (CL) emission of sample CEBP035, the crystal domains in grain G01 display only subtle luminescence contrast (Figure 4B). Spot 1 (~146.0 ppm U) is located centrally within the brighter CL domain, whereas Spot 2 (~28.7 ppm U) is positioned near the grain margin, straddling the boundary between the brighter core and the darker lateral domain. Because this low luminescence contrast alone does not allow a clear distinction between compositional zoning and structural features, high-resolution Raman mapping was used to evaluate crystal lattice strain across these domains.

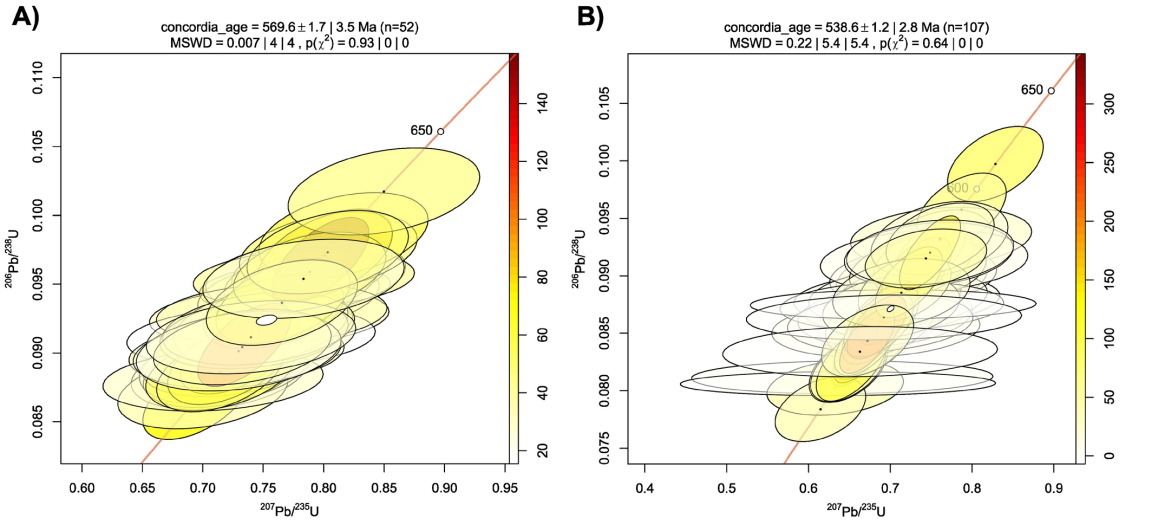


Figure 3. Wetherill concordia diagrams for apatite U-Pb age data. (A) Sample BJ19C yielding a concordia age of 569.6 ± 1.7 Ma. (B) Sample CEBP035 yielding a concordia age of 538.6 ± 1.2 Ma. The color scale represents uranium concentration (U, ppm) for each analytical spot.

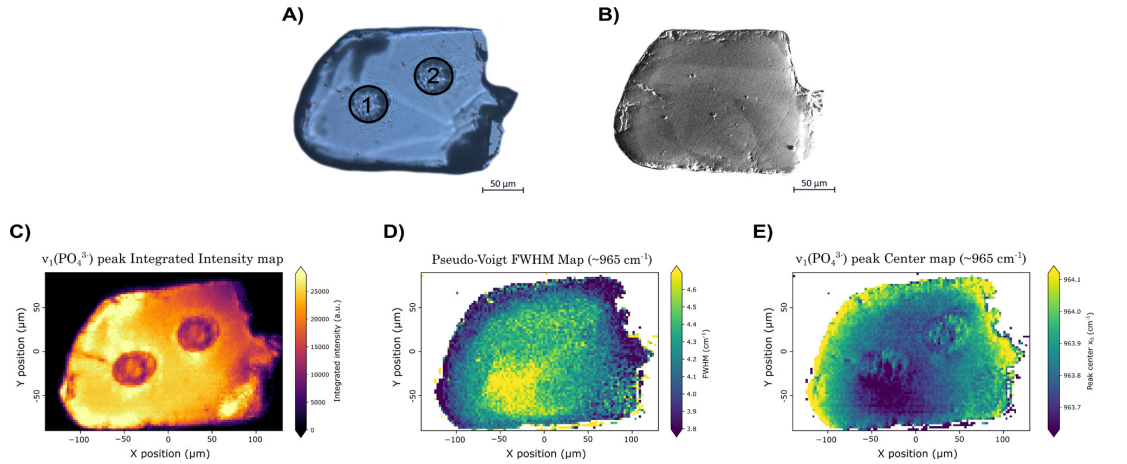


Figure 4. Multi-analytical characterization of apatite grain CEBP035-G01. (A) Transmitted-light image showing the grain and LA-ICP-MS ablation spots. (B) Cathodoluminescence (CL) image highlighting internal luminescence variations. (C) Raman intensity map indicating signal intensity and ablation pit locations. (D) Raman FWHM map showing spatial variations in lattice disorder. (E) Raman peak position map showing spatial variations in peak center position across the grain.

The structural response associated with localized chemical variability was evaluated using high-resolution Raman mapping of the ν_1 (PO_4) symmetric stretching mode (≈ 965 cm^{-1}). Spatial variations observed in cathodoluminescence (CL) are spatially associated with subtle differences in Raman peak broadening. Spot G01-1 (≈146.0 ppm U), located within the brighter CL domain, exhibits a higher Full Width at Half Maximum (FWHM ≈ 4.4 cm^{-1}) compared with spot G01-2 (≈ 28.7 ppm U; FWHM ≈ 3.2 cm^{-1}) (Figure 4D). This systematic peak broadening is consistent with localized lattice strain and structural distortion associated with uranium enrichment.

Raman FWHM values provide a sensitive indicator of lattice disorder, as progressive alpha-decay damage in phosphate minerals promotes vibrational band broadening due to increasing structural distortion. For comparison, thermally annealed Durango apatite has been reported to exhibit FWHM values of approximately 4.64 cm^{-1}, whereas natural Durango apatite with low accumulated radiation damage shows average values of approximately 4.96 cm^{-1} [22]. In contrast, highly damaged or amorphized phosphate structures exhibit pronounced peak broadening and loss of well-defined vibrational features. The FWHM values measured across apatite grain CEBP035-G01 (3.2-4.4 cm^{-1}) are consistent with a largely crystalline phosphate framework and do not indicate extensive radiation-induced amorphization. Therefore, although the U-rich domain exhibits increased lattice disorder relative to the lower-U domain, the apatite structure remains largely preserved despite localized uranium enrichment. However, because FWHM values are sensitive to instrument-specific spectral resolution and local compositional variations, no transferable operational threshold can presently be proposed for classifying preserved versus degraded domains; such calibrations must remain instrument- and sample-specific.

In the Raman intensity map (Figure 4C), localized signal attenuation is observed at the ablation sites, which is interpreted as an optical artifact caused by variations in laser focusing conditions due to pit topography rather than internal lattice modification. In contrast, in the Raman FWHM map (Figure 4D), no obvious FWHM anomaly spatially coincident with the pits was resolved at the mapping resolution, suggesting that the ablation process did not induce widespread structural disorder across the analyzed volume.

The Raman peak position map (Figure 4E), corresponding to the v1 PO_4 stretching band at approximately 965 cm^{-1}, reveals systematic peak shifts that spatially correlate with the regions of elevated FWHM values in Figure 4D. As radiation damage accumulates, defects and local distortions in the apatite crystal lattice alter the vibrational environment of the phosphate tetrahedra, producing shifts in the Raman band position. These structural modifications reflect changes in bond lengths and interatomic force constants associated with lattice disorder, directly modifying the vibrational frequencies of the phosphate framework. However, peak position shifts in apatite can also reflect subtle compositional variations, such as localized halogen or trace element substitutions[22]. Therefore, while peak position shifts cannot be attributed solely to metamictization, the close spatial correspondence between the peak position and FWHM maps provides evidence consistent with radiation-induced structural strain rather than analytical artifacts.

Altogether, these results indicate that localized uranium enrichment in grain G01 produces measurable lattice strain without causing extensive structural degradation. However, because high-resolution Raman mapping was conducted on a single representative grain, this analysis should be considered a detailed proof-of-concept case study. Additional Raman mapping across multiple grains will be necessary to establish broader relationships between uranium/thorium distribution, radiation damage, lattice strain, and isotopic retentivity.

3.6. Zircon U-Pb geochronology and radiation damage

Unlike the structural resilience observed in Brazilian apatite, the Archean zircon samples from the Carajás Province (C16, C20, and C23; > 2.7 Ga) exhibit variable degrees of lattice degradation accumulated over geological timescales. In the context of a fission-track and U-Pb double-dating approach, surface etching served a dual methodological purpose, functioning as a physical structural screening tool prior to in situ LA-ICP-MS U-Pb dating.

To evaluate the impact of etching on metamict zircon systematics, analytical results from unetched and etched aliquots were compared across all three Archean samples (Table 3).

Transmitted-light photomicrographs of the etched zircon grains illustrate the spatial variability of radiation-damage-induced corrosion across different intra-crystalline domains (Figure 5). The LA-ICP-MS ablation spots were systematically targeted in areas displaying moderate etching, characterized by the clear presence of revealed fission tracks while avoiding severely corroded and structurally degraded domains. In sample C16 (Figure 5A), etching reveals a sharp contrast between a heavily corroded domain and a zone containing revealed tracks where the ablation spot was placed.

Table 3. Summary of U-Pb zircon isotopic results and upper-intercept ages obtained from discordia regressions before and after etching treatment.

Sample	Condition	n	Upper Intercept (Ma)	± 2σ (Ma)	$MSWD_{conc}$	$MSWD_{disc}$
C16	Unetched	28	2778.0	24.0	130.0	1.50
	Etched	45	2760.0	9.0	85.0	0.42
C20	Unetched	22	2730.8	9.6	0.67	0.62
	Etched	21	2746.0	12.0	83.0	0.55
C23	Unetched	31	2743.0	11.0	86.0	0.47
	Etched	34	2743.0	11.0	85.0	0.70

Note: n = number of analytical points obtained by LA-ICP-MS; Upper Intercept = Upper intercept age. $MSWD_{conc}$: Mean Square of Weighted Deviates calculated by testing the hypothesis of an equivalent population/single concordia point[37]. $MSWD_{disc}$: MSWD of the upper-intercept discordia regression[36].

Similarly, samples C20 (Figure 5B) and C23 (Figure 5C) exhibit heterogeneous etching responses, displaying regions of intense degradation alongside domains with distinct fission tracks suitable for analytical targeting.

The comparison between unetched and etched zircon aliquots reveals distinct patterns in isotopic behavior across the analyzed samples. In unetched grains, the absence of chemical revelation limits the identification of intra-crystalline variations in radiation damage, resulting in a higher probability of sampling domains with contrasting structural conditions during LA-ICP-MS analysis. Consequently, analytical spots may encompass mixtures of structurally preserved regions and radiation-damaged domains that are more susceptible to radiogenic Pb loss.

In contrast, etching preferentially reveals and removes structurally compromised domains associated with radiation damage. These domains are commonly characterized by enhanced susceptibility to Pb loss and isotopic disturbance. Following the structural classification proposed by Azevedo[13], this treatment enables the distinction between relatively preserved regions—characterized by homogeneous fission-track revelation and limited surface degradation—and damaged or anomalous zones. By targeting LA-ICP-MS analyses within the preserved regions identified after etching, the contribution of highly degraded domains is minimized. Rather than systematically reducing isotopic dispersion, the etching treatment redistributes analytical points along the discordia vector, which can enhance age constraints in highly discordant crystals while preserving statistically equivalent upper-intercept ages (Table 3).

In sample C16, the unetched population defined a linear discordia with an upper intercept age of 2778.0 ± 24.0 Ma ($MSWD_{disc}$ = 1.50; $MSWD_{conc}$ = 130.0) (Figure 6A). In the aliquot subjected to etching, the upper intercept was determined at 2760.0 ± 9.0 Ma ($MSWD_{disc}$ = 0.42 ; $MSWD_{conc}$ = 85.0) (Figure 6B). The deviation between upper intercepts (age offset) was −18.0 Ma, accompanied by a substantial reduction in analytical uncertainty from ±24.0 Ma down to ±9.0 Ma.

For sample C20, the unetched population yielded an upper intercept age of 2730.8 ± 9.6 Ma ($MSWD_{disc}$ = 0.62 ; $MSWD_{conc}$ = 0.67) (Figure 6C). In the etched aliquot, the upper intercept shifted to 2746.0 ± 12.0 Ma ($MSWD_{disc}$ = 0.55; $MSWD_{conc}$ = 83.0), recording a positive age offset of +15.2 Ma (Figure 6D).

Sample C23 exhibited identical upper intercept ages across both aliquots, fixed at 2743.0 ± 11.0 Ma (Figure 6EF). The linear discordia regressions yielded $MSWD_{disc}$ values of 0.47 for unetched grains and 0.70 for etched grains, contrasting with the elevated $MSWD_{conc}$ values (86.0 and 85.0, respectively) obtained from the single-population concordia model. These results indicate that the datasets are not statistically consistent with a single concordant population.

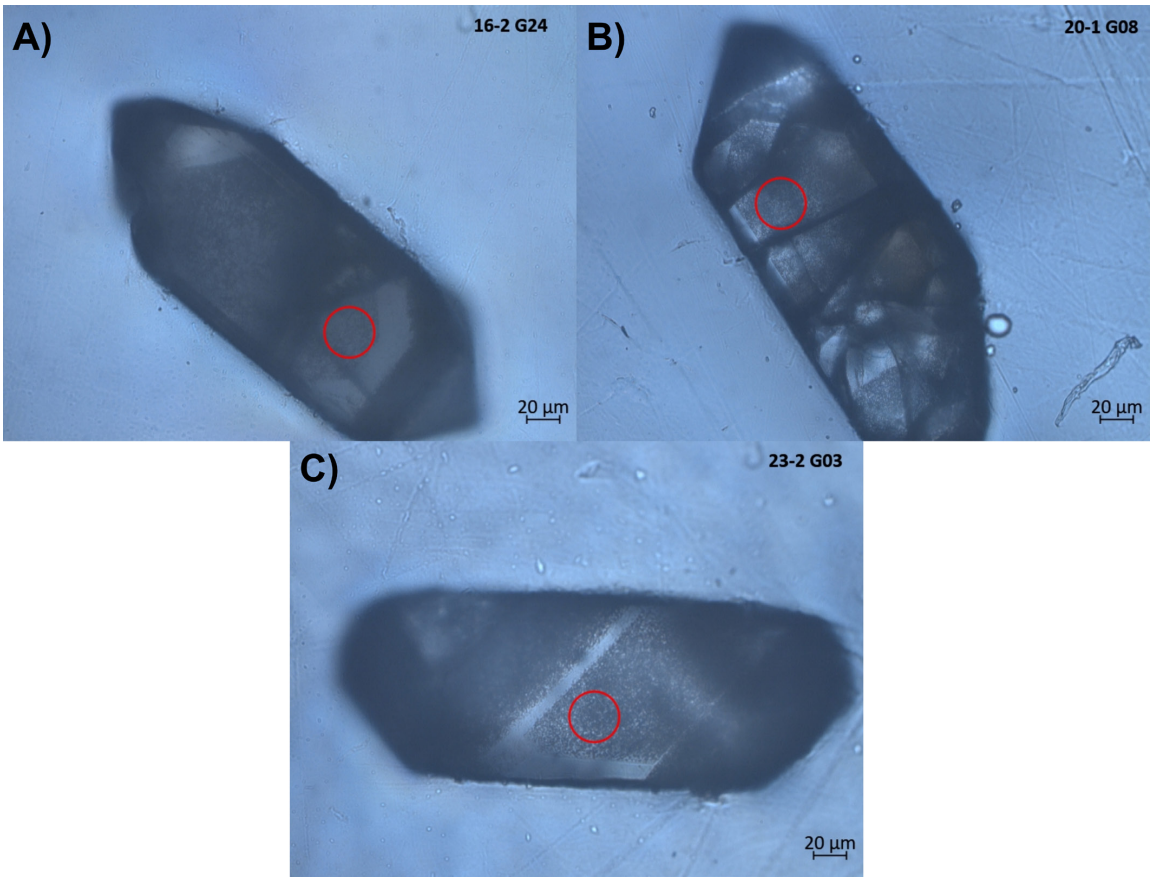


Figure 5. Transmitted-light photomicrographs of chemically etched Archean zircons showing LA-ICP-MS ablation spots (red circles): (A) Sample C16 grain; (B) Sample C20 grain; (C) Sample C23 grain.

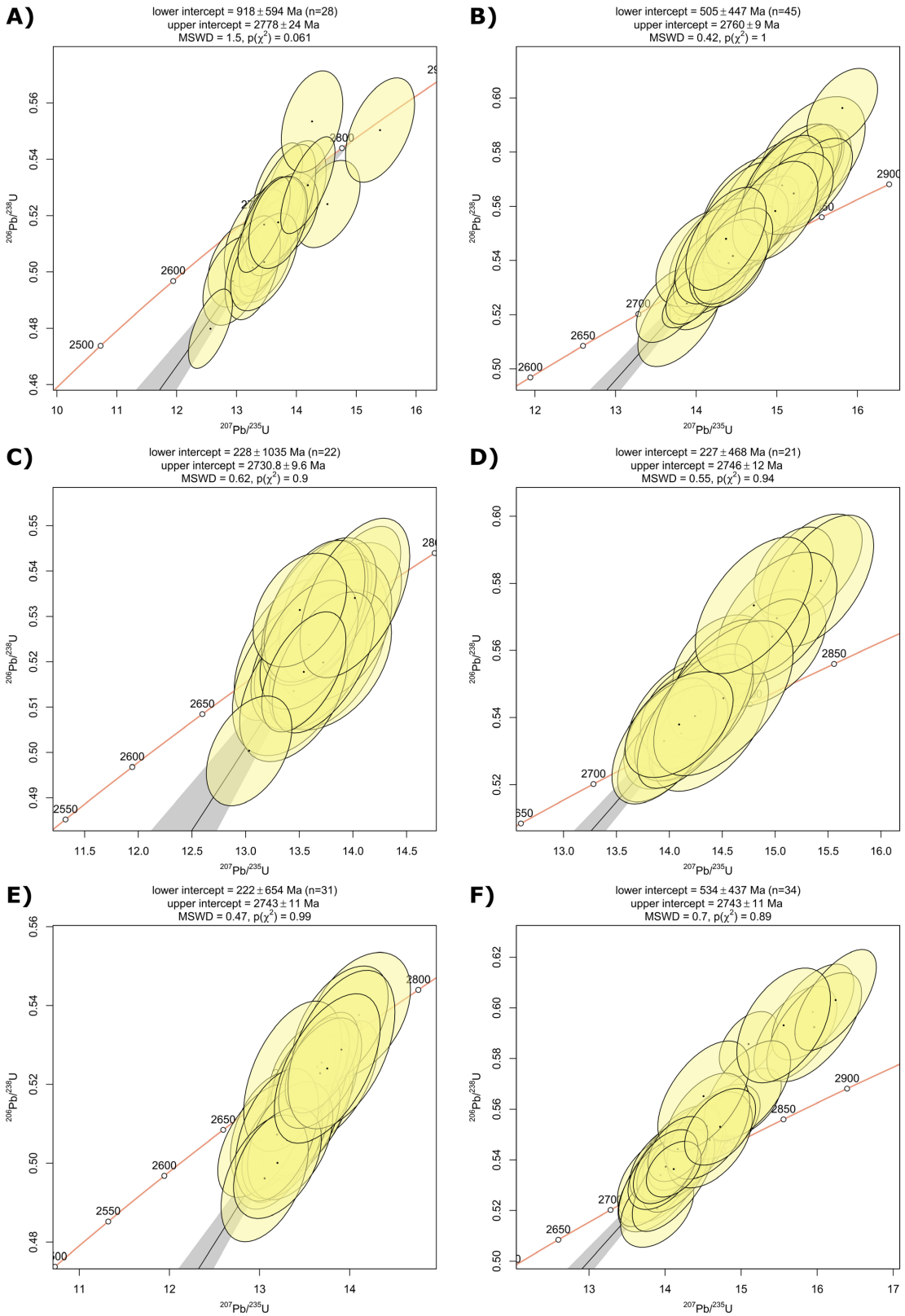


Figure 6. Wetherill U-Pb concordia diagrams for Archean zircon samples C16, C20, and C23. For each sample, the unetched population is shown in the left panel and the etched population in the right panel: (A) unetched and (B) etched C16; (C) unetched and (D) etched C20; (E) unetched and (F) etched C23.

The isotopic response of Archean zircons from the Carajás Mineral Province (> 2.7 Ga) underscores the necessity of linear discordia regressions over single-population concordia age models. Accumulated alpha-decay damage over geological timescales may promote open-system behavior and increase susceptibility to radiogenic Pb loss. Applying a single-population concordia model to such datasets yields artificially high dispersion ($MSWD_{conc} = 80 - 130$) because the analytical spots define a lead-loss trend rather than a single undisturbed concordant cluster.

When evaluated via linear discordia regressions, both unetched and etched populations define robust linear arrays with $MSWD_{disc} \leq 1.50$, consistent with regional Pb-loss trajectories reported in the Carajás Province[26]. In both unetched and etched aliquots, most analyses remain below the concordia curve and define similarly oriented discordia trends. Etching therefore redistributes the analytical points along a comparable discordia trajectory rather than generating a fundamentally different discordance pattern.

Crucially, despite this redistribution of data points along the discordia vector, both etched and unetched populations anchor to statistically equivalent upper-intercept ages within analytical uncertainty (e.g., 2778 ± 24 Ma unetched vs. 2760 ± 9 Ma etched for sample C16). This spatial alignment confirms that, although etching modifies the distribution of intra-grain isotopic ratios along the discordia trajectory, it does not significantly alter the upper-intercept crystallization ages within analytical uncertainty.

4. Conclusions

The integrated characterization of apatite and zircon crystal lattices demonstrates that the stability and reliability of the U-Pb isotopic system are strongly influenced by the physical and crystallographic state of the mineral. Internal chemical gradients and cumulative radiation damage generate complex microscale structural variations within these accessory phases. These heterogeneities contribute to isotopic dispersion, highlighting that understanding microstructural integrity is an important prerequisite for the accurate interpretation of in situ geochronological data.

In the Borborema Province apatites, geochronological behavior and isotopic stability are closely linked to chemical variations and uranium zoning, although this relationship cannot be reduced to a simplistic, linear "high-U equals younger-age" correlation at the single-spot level. For instance, the visually homogeneous sample BJ19C, characterized by a uniform distribution of fission tracks, yields an exceptionally stable and concordant population age of 569.6 ± 1.7 Ma with an extremely low bulk MSWD of 0.007, yet its individual spot analyses exhibit a real age dispersion (535.4 to 623.1 Ma) that exceeds analytical uncertainty. This pattern demonstrates that an extremely low MSWD reflects under-dispersion relative to assigned uncertainties rather than true isotopic homogeneity across the analyzed domains. Conversely, the highly zoned sample CEBP035 shows extreme uranium variations (5.94 to 329.79 ppm) and wide age dispersion (487.9 to 614.5 Ma), with severe intra-grain offsets, demonstrating that major chemical gradients are associated with significant isotopic disturbance. However, three-dimensional zoning, common Pb corrections, and complex diffusion pathways complicate direct spot-by-spot age predictions.

Providing a physical context for these observations, high-resolution Raman mapping of representative grain CEBP035-G01 provides a microstructural link between chemical heterogeneity and lattice response. It demonstrates that uranium-rich domains experience localized lattice strain, documented by broadening of the ν_1 (PO_4) stretching peak (FWHM increasing from 3.2 to 4.4 cm^{-1}), while the overall phosphate framework remains largely crystalline. This indicates that significant isotopic disturbance and age dispersion can occur along steep chemical gradients without requiring extensive lattice amorphization. Nonetheless, because this spectroscopic mapping was conducted on a single grain, it must be treated strictly as a detailed proof-of-concept. Future systematic studies across larger crystal populations are required to calibrate Raman spectroscopy as a predictive diagnostic tool for isotopic stability.

For the Archean zircons of the Carajás Province (>2.7 Ga), progressive radiation damage promotes metamictization, open-system behavior, and Pb loss. Etching preferentially attacks structurally compromised domains, allowing relatively preserved regions to be identified for subsequent LA-ICP-MS targeting. In the etched aliquots, analytical spots plotted along similarly oriented discordia trends compared to unetched populations, without altering the overall vector. Most points remain below concordia in both populations, preserving the dominant normal Pb-loss discordance. However, isotopic patterns between aliquots are strongly sample-dependent: while the etched population of sample C16 exhibited a tighter alignment and improved regression precision, the etched aliquot of C20 displayed a wider spatial distribution of analytical spots along the discordia trajectory. Crucially, this wider distribution along the loss vector in C20 did not degrade the linear fit. Recognizing that differences between aliquots reflect both etching effects and natural inter-grain variability, these results indicate that linear discordia regressions provide a more robust framework than single-population concordia models for interpreting partially metamict zircon populations.

In summary, this study highlights that geochronological interpretations in accessory minerals with complex chemical zoning and radiation histories depend strongly on the spatial targeting and characterization of chemically and structurally heterogeneous domains. Controlled chemical etching in metamict zircon serves as a useful pre-analytical screening tool to visually identify and avoid severely corroded domains during LA-ICP-MS spot placement; however, it cannot be regarded as a universal method for improving U-Pb precision or accuracy across all populations. Because isotopic responses are sample-dependent and reflect both chemical treatment and natural inter-grain variability, pre-analytical screening should be integrated with appropriate geochronological models. Combining microstructural characterization such as Raman mapping for apatite and surface-etch screening for zircon provides a framework for interpreting complex U-Pb datasets in partially metamict accessory phases.

5. Acknowledgments

Financial support for this research was provided by the São Paulo Research Foundation (FAPESP) through grants 2023/18307-7 and 2024/20042-4. The authors also acknowledge the Graduate Program in Materials Science and Technology (POSMAT) at São Paulo State University (UNESP) for institutional support. Furthermore, recognition is extended to the London Geochronology Centre (UCL) for providing analytical facilities, technical assistance, and expertise in data processing.

6. Data Availability

The raw and processed data supporting the findings of this study are available from the corresponding author upon reasonable request.

7. Supplementary Material

The following online material is available for this article:

Table S1 - LA-ICP-MS U–Pb analytical data and fission-track parameters for selected apatite grains from sample BJ19C.

Table S2 - LA-ICP-MS U–Pb analytical data and fission-track parameters for selected apatite grains from sample CEBP035.

8. References

1. Price PB, Walker RM. A simple method of measuring low uranium concentrations in natural crystals. Appl Phys Lett. 1963;2(2):23-5. https://doi.org/10.1063/1.1753753.
2. Fleischer RL, Price PB, Walker RM. Nuclear tracks in solids. Berkeley: University of California Press; 1975. https://doi.org/10.1525/9780520320239.
3. Wagner GA, Van den Haute P. Fission-track dating. Dordrecht: Springer Netherlands; 1992. https://doi.org/10.1007/978-94-011-2478-2.
4. Nasdala L, Wenzel M, Vavra G, Irmer G, Wenzel T, Kober B. Metamictisation of natural zircon: accumulation versus thermal annealing of radioactivity-induced damage. Contrib Mineral Petrol. 2001;141(2):125-44. https://doi.org/10.1007/s004100000235.
5. Donelick RA, O'Sullivan PB, Ketcham RA. Apatite fission-track analysis. Rev Mineral Geochem. 2005;58(1):49-94. https://doi.org/10.2138/rmg.2005.58.3.
6. Chew DM, Donelick RA. Combined apatite fission track and U-Pb dating by LA-ICP-MS and its application in apatite provenance analysis. Mineral Assoc Can Short Course. 2012;42:219-47. https://doi.org/10.3749/9780921294825.ch12.
7. Gleadow AJW, Seiler C. Fission track dating and thermochronology. In: Jack Rink W, Thompson JW, editors. Encyclopedia of Scientific Dating Methods. Dordrecht: Springer Netherlands; 2015. p. 285-96. https://doi.org/10.1007/978-94-007-6304-3_5.
8. Ketcham RA, Guenthner WR, Reiners PW. Geometric analysis of radiation damage connectivity in zircon, and its implications for helium diffusion. Am Mineral. 2013;98(2-3):350-60. https://doi.org/10.2138/am.2013.4249.
9. Chew DM, Spikings RA. Geochronology and thermochronology using apatite: time and temperature, lower crust to surface. Elements (Que). 2015;11(3):189-94. https://doi.org/10.2113/gselements.11.3.189.
10. Malusà MG, Fitzgerald PG. Fission-track thermochronology and its application to geology. Cham: Springer International Publishing; 2019. https://doi.org/10.1007/978-3-319-89421-8.
11. Holland HD, Gottfried D. The effect of nuclear radiation on the structure of zircon. Acta Crystallogr. 1955;8(6):291-300. https://doi.org/10.1107/S0365110X55000947.
12. Guenthner WR, Reiners PW, Ketcham RA, Nasdala L, Giester G. Helium diffusion in natural zircon: radiation damage, anisotropy, and the interpretation of zircon (U-Th)/He thermochronology. Am J Sci. 2013;313(3):145-98. https://doi.org/10.2475/03.2013.01.
13. Azevedo MC. Caracterização Cristalográfica e Isotópica do Mineral Zircão Através do Método de Traços De Fissão, U-Pb e U-Th/He: Geocronologia da Província Borborema, RN, Brasil [thesis]. Presidente Prudente: Universidade Estadual Paulista; 2021.
14. Chew DM, Petrus JA, Kamber BS. U-Pb LA-ICPMS dating using accessory mineral standards with variable common Pb. Chem Geol. 2014;363:185-99. https://doi.org/10.1016/j.chemgeo.2013.11.006.
15. Shuster DL, Flowers RM, Farley KA. The influence of natural radiation damage on helium diffusion kinetics in apatite. Earth Planet Sci Lett. 2006;249(3-4):148-61. https://doi.org/10.1016/j.epsl.2006.07.028.
16. Flowers RM, Ketcham RA, Shuster DL, Farley KA. Apatite (U-Th)/He thermochronometry using a radiation damage accumulation and annealing model. Geochim Cosmochim Acta. 2009;73(8):2347-65. https://doi.org/10.1016/j.gca.2009.01.015.
17. Tello Sáenz CA, Curvo EA, Dias AN, Soares CJ, Constantino CJL, Alencar I, et al. Effects of etching on zircon grains and its implications for the fission track method. Appl Spectrosc. 2012;66(5):545-51. https://doi.org/10.1366/11-06260. PMid:22524960.
18. Resende RS, Sáenz CAT, Pereira LAS, Dantas EL. The effect of chemical and physical imperfections in zircon grains in influencing the U-Pb age analyses: insights from zircon fission track etching. Lithos. 2019;346-347:105138. https://doi.org/10.1016/j.lithos.2019.07.005.
19. Horstwood MSA, Košler J, Gehrels G, Jackson SE, McLean NM, Paton C, et al. Community-Derived Standards for LA-ICP-MS U-(Th-)Pb Geochronology - Uncertainty Propagation, Age Interpretation and Data Reporting. Geostand Geoanal Res. 2016;40(3):311-32. https://doi.org/10.1111/j.1751-908X.2016.00379.x.
20. Antonakos A, Liarokapis E, Leventouri T. Micro-Raman and FTIR studies of synthetic and natural apatites. Biomaterials. 2007;28(19):3043-54. https://doi.org/10.1016/j.biomaterials.2007.02.028. PMid:17382382.
21. Resende RS, Sáenz CAT, Curvo EAC, Constantino CJL, Aroca RF, Nakasuga WM. Raman spectroscopy and scanning electron microscopy characterizations of fission track method datable zircon grains. Appl Spectrosc. 2014;68(5):549-56. https://doi.org/10.1366/13-07302. PMid:25014598.
22. Zeng X, Pastore G, Shen C, Resentini A, Fu H, Yang C, et al. Raman mapping reveals alpha radiation damage zonation and its annealing in Durango apatite. Earth Planet Sci Lett. 2025;671:119636. https://doi.org/10.1016/j.epsl.2025.119636.
23. Dantas EL, Van Schmus WR, Hackspacher PC, Fetter AH, Neves BBB, Cordani U, et al. The 3.4-3.5 Ga São José do Campestre massif, NE Brazil: remnants of the oldest crust in South America. Precambrian Res. 2004;130(1-4):113-37. https://doi.org/10.1016/j.precamres.2003.11.002.
24. Pinéo TRG, Costa FG, Basto CF, Rodrigues JB, Medeiros VC, Palheta ESM, et al. New zircon U-Pb dating and review of geological and geochronological data with implications for lithostratigraphy and crustal evolution of North Borborema Province, northeastern Brazil. J Geol Surv Braz. 2022;6(1):23-41. https://doi.org/10.29396/jgsb.2023.v6.n1.3.
25. Caxito FA, Santos LCML, Ganade CE, Bendaoud A, Fettous EH, Bouyo MH, et al. Toward an integrated model of geological evolution for NE Brazil-NW Africa: The Borborema Province and its connections to the Trans-Saharan and Central African

orogens. Braz J Geol. 2020;50(2):e20190122. https://doi.org/10.1590/2317-4889202020190122.

26. Moreto CPN, Monteiro LVS, Xavier RP, Amaral WS, Santos TJS, Juliani C, et al. Mesoarchean (3.0 and 2.86 Ga) host rocks of the iron oxide-Cu-Au Bacaba deposit, Carajás Mineral Province: U-Pb geochronology and metallogenetic implications. Miner Depos. 2011;46(7):789-811. https://doi.org/10.1007/s00126-011-0352-9.
27. Cherniak DJ, Lanford WA, Ryerson FJ. Lead diffusion in apatite and zircon using ion implantation and Rutherford Backscattering techniques. Geochim Cosmochim Acta. 1991;55(6):1663-73. https://doi.org/10.1016/0016-7037(91)90137-T.
28. Carlson WD, Donelick RA, Ketcham RA. Variability of apatite fission-track annealing kinetics; I, experimental results. Am Mineral. 1999;84(9):1213-23. https://doi.org/10.2138/am-1999-0901.
29. Gleadow AJW, Hurford AJ, Quaife RD. Fission track dating of zircon: improved etching techniques. Earth Planet Sci Lett. 1976;33(2):273-6. https://doi.org/10.1016/0012-821X(76)90235-1.
30. Thomson SN, Gehrels GE, Ruiz J, Buchwaldt R. Routine low-damage apatite U-Pb dating using laser ablation-multicollector-ICPMS. Geochem Geophys Geosyst. 2012;13(2):Q02009. https://doi.org/10.1029/2011GC003928.
31. McDowell FW, McIntosh WC, Farley KA. A precise 40Ar-39Ar reference age for the Durango apatite (U-Th)/He and fission-track dating standard. Chem Geol. 2005;214(3-4):249-63. https://doi.org/10.1016/j.chemgeo.2004.10.002.
32. Soares CJ, Mertz-Kraus R, Guedes S, Stockli DF, Zack T. Characterisation of Apatites as Potential Uranium Reference Materials for Fission-track Dating by LA-ICP-MS. Geostand Geoanal Res. 2015;39(3):305-13. https://doi.org/10.1111/j.1751-908X.2014.00301.x.
33. Sláma J, Košler J, Condon DJ, Crowley JL, Gerdes A, Hanchar JM, et al. Plešovice zircon: a new natural reference material for U-Pb and Hf isotopic microanalysis. Chem Geol. 2008;249(1-2):1-35. https://doi.org/10.1016/j.chemgeo.2007.11.005.
34. Wiedenbeck M, Allé P, Corfu F, Griffin WL, Meier M, Oberli F, et al. Three natural zircon standards for U-Th-Pb, Lu-Hf, trace element and REE analyses. Geostand Newsl. 1995;19(1):1-23. https://doi.org/10.1111/j.1751-908X.1995.tb00147.x.
35. Vermeesch P. KJ: A Julia package for physics-based LA-ICP-MS data processing. In: Goldschmidt 2025 Conference; 2025 July 6-11; Prague, Czech Republic. Proceedings. Amsterdam: European Association of Geochemistry and the Geochemical Society; 2025. https://doi.org/10.7185/gold2025.30135.
36. Vermeesch P. IsoplotR: A free and open toolbox for geochronology. Geoscience Frontiers. 2018;9(5):1479-93. https://doi.org/10.1016/j.gsf.2018.04.001.
37. Ludwig KR. On the treatment of concordant uranium-lead ages. Geochim Cosmochim Acta. 1998;62(4):665-76. https://doi.org/10.1016/S0016-7037(98)00059-3.